Supporting Information

Synergetic Spin-Valence Catalysis Mechanism in Oxygen Reduction Reactions on Fe-N-C Single-Atom Catalysts

Daoxiong Wu[a], Zhiwen Zhuo[b], Yiming Song[a], Peng Rao[a], Junming Luo[a], Jing Li[a], Peilin Deng[a*], Jinlin Yang[a],

Xiaojun Wu[c], and Xinlong Tian[a*]

[a] State Key Laboratory of Marine Resource Utilization in South China Sea, Hainan Provincial Key Lab of

Fine Chemistry, School of Chemical Engineering and Technology, Hainan University, Haikou 570228, China

[b] Anhui Province Key Laboratory of Optoelectric Materials Science and Technology, Key Laboratory of Functional Molecular

Solids Ministry of Education, and Department of Physics, Anhui Normal University, Wuhu, Anhui, 241000, China

[c] Hefei National Research Center for Physical Sciences at the Microscale, Collaborative Innovation Center

of Chemistry for Energy Materials, CAS Key Laboratory of Materials for Energy Conversion, CAS Center for

Excellence in Nanoscience, and School of Chemistry and Materials Sciences, University of Science and

Technology of China, Hefei, Anhui 230026, China

Corresponding authors: *dengpeilin@hainanu.edu.cn (P. Deng); tianxl@hainanu.edu.cn (X. Tian)*

Calculations Details

Spin-polarized density functional theory calculations were performed using the Perdew-Burke-Ernzerhof (PBE)[1] functional and the projector augmented wave (PAW)[2,3] potential as implemented in the Vienna Ab Initio Simulation Package (VASP).[4,5] The C, N, Fe_sv, O, Cl, and H POTCAR files are used in our calculations. An energy cutoff of 520 eV and a convergence criterion of 10^{-5} eV for self-consistent calculations was adopted. All structures were fully relaxed until the total force on each atom was less than 0.01 eV/Å. The thickness of the vacuum layer was large than 14 Å. Our single-atom catalyst models were built based on 6 × 6 × 1 graphene supercells. A Γ-centered k-point of 3 × 3 × 1 was adopted. The DFT-D3 method with Becke-Jonson damping is used to add vdW dispersion correction.[6] The solvent effect was included by using the implicit solvation model as implemented in the VASPsol code.[7,8] Our test calculations (Figure S9) show that the ΔG_{OH*} for Fe–N$_4$–C based on implicit solvation model (ΔG_{OH*} = 0.50 eV) is closed to that based on the combination of explicit solvation model and implicit solvation model (ΔG_{OH*} = 0.47 eV), indicating that the results based on implicit solvation model are reasonable. The Def2-TZVP basis set[9] was used in the SSAdNDP calculations.[10] VASPKIT code[11] and VESTA software[12] were used for calculation pre-processing and post-processing.
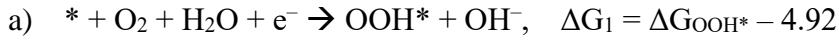
The U_{eff} = U – J = 3 eV were applied to Fe_*d* orbitals.[13] The ΔE_{spin} of low-spin, medium-spin, and high-spin Fe–N$_4$–C based on HSE06 functional of 578, 0, 701 eV, respectively, which is comparable to those based on U_{eff} = 3eV (ΔE_{spin} = 536, 0, and 786 eV for LS, MS, HS, respectively). Moreover, the ΔG_{OH*} in the EF pathway in Fe–N$_4$–C based on HSE06 is 0.58 eV, comparable to that based on U_{eff} = 3eV (0.50 eV). Hence, the U_{eff} = 3eV setting can reliably determine the magnetic ground state and the reactivity of the Fe cations in our models.

The computational hydrogen electrode (CHE) model[14] was used in our calculations. The Gibbs free energy of molecules and ORR-related adsorbates was calculated by:

$$G = E_{DFT} + ZPE - TS \qquad (1)$$

where E_{DFT}, ZPE, and S were the DFT energy, zero-point energy, and entropy, respectively, and temperature

T was adopted as 298.15 K. The ORR involves four electron steps:

a) $* + O_2 + H_2O + e^- \rightarrow OOH* + OH^-$, $\Delta G_1 = \Delta G_{OOH*} - 4.92$

b) $OOH* + e^- \rightarrow O* + OH^-$, $\Delta G_2 = \Delta G_{O*} - \Delta G_{OOH*}$

c) $O* + H_2O + e^- \rightarrow OH* + OH^-$, $\Delta G_3 = \Delta G_{OH*} - \Delta G_{O*}$

d) $OH* + e^- \rightarrow OH^- + *$, $\Delta G_4 = - \Delta G_{OH*}$

The ΔG_{OOH*}, ΔG_{O*}, and ΔG_{OH*} are calculated according to:

a) $\Delta G_{OOH*} = G(OOH*) - G(*) + 1.5 \times G(H_2) - 2 \times G(H_2O)$

b) $\Delta G_{O*} = G(O*) - G(*) + G(H_2) - G(H_2O)$

c) $\Delta G_{OH*} = G(OH*) - G(*) + 0.5 \times G(H_2) - G(H_2O)$

Constant-potential Simulations

The electric potential of the single-atom catalyst models referenced to the standard hydrogen electrode (SHE) and reversible hydrogen electrode (RHE) could be calculated by:

$$U_{SHE} = W_f/e - W_H/e \tag{2}$$

$$U_{RHE} = U_{SHE} + 0.0592 \times pH \tag{3}$$

where the W_f is the calculated work function of the single-atom catalyst models, W_H is the work function of H_2/H^+ couple at standard conditions adopted as 4.60 eV,[15] and pH is the pH values. The U_{SHE} could be controlled by adjusting the numbers of doping charges in the catalyst models. For each models, nine calculations are performed at charges of -2.0e to +2.0e with steps of +0.5e. In the constant-potential simulations, the spin states of Fe cations are constrained by using the occupation matrix plugin developed by Watson group.[16] Then the potential-dependent free energy ($E_{free}(U_{SHE})$) could be calculated by:[17]

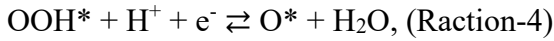$$E_{free}(U_{SHE}) = E_{DFT} + \int_0^q \langle \overline{V_{tot}} \rangle dQ + qW_f/e \tag{4}$$
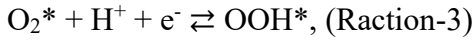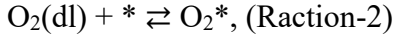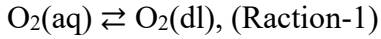
where the E_{DFT} is the calculated DFT energy, $\langle \overline{V_{tot}} \rangle$ is the averaged electrostatic potential of the model, and q is the doping charge. The E_{free} and U_{SHE} can be fitted to a quadratic function:

$$E_{free}(U_{SHE}) = -0.5 \times C \times (U_{SHE} - U_{PZC})^2 + E_0 \tag{5}$$

where three fitting parameters C, U_{PZC}, and E_0 refers to the capacitance of the surface, the potential of zero charge (PZC), and the energy at the PZC, respectively. The E_{free} then replaces the E_{DFT} in the formula (1) to obtain the potential-dependent free energy of *, OOH*, O*, and OH*.

Microkinetic Simulations:

The intermediate reactions considered are:

$O_2(aq) \rightleftarrows O_2(dl)$, (Raction-1)

$O_2(dl) + * \rightleftarrows O_2*$, (Raction-2)

$O_2* + H^+ + e^- \rightleftarrows OOH*$, (Raction-3)

$OOH* + H^+ + e^- \rightleftarrows O* + H_2O$, (Raction-4)

$O* + H^+ + e^- \rightleftarrows OH*$, (Raction-5)

$OH* + H^+ + e^- \rightleftarrows H_2O + *$, (Raction-6)
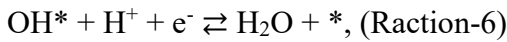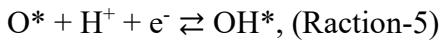
For Reaction-i, k_i and K_i are forward rate constant and equilibrium constant, respectively. Backward rate constant (k_{-i}) is $k_{-i} = k_i/K_i$. For thermochemical steps (Raction-1 and Raction-2), the k_i and K_i are:

$$k_i = A_i \exp\left(-\frac{\Delta G_{a,i}}{k_b T}\right) \qquad (6)$$

$$K_i = \exp\left(-\frac{\Delta G_i}{k_b T}\right) \qquad (7)$$

where the A_i, $\Delta G_{a,i}$, ΔG_i, and k_b are the prefactor, activation free energy, reaction free energy, and Boltzmann constant, respectively. A_1, A_2, A_3, A_4, A_5, and A_6 are adopted as 8×10^5, 10^8, 10^9, 10^9, 10^9, and 10^9,[18] respectively. For electrochemical reduction steps (From Raction-3 to Raction-6), the k_i and K_i are:

$$k_i = A_i \exp\left[-\frac{\Delta G_{a0,i} + \beta_i(\Delta G_{0,i} + eU)}{k_b T}\right] \qquad (8)$$

$$K_i = \exp\left(-\frac{\Delta G_{0,i} + eU}{k_b T}\right) \qquad (9)$$

where $\Delta G_{a0,i}$, $\Delta G_{0,i}$, and β_i are the activation free energy at U (vs RHE) = 0 V, the reaction free energy at U (vs RHE) = 0 V, and transfer coefficient adopted as 0.5,[18] respectively. $\Delta G_{a0,i}$ is generally small, ranging between 0.15 eV and 0.28 eV.[19] The value $\Delta G_{a0,i}$ is taken as 0.26 eV, which has been adopted by many theoretical researches.[19-23]

The reaction rates of each elementary step are:

$r_1 = k_1 \chi_{O2\_aq} - k_{-1} \chi_{O2\_dl}$

$$r_2 = k_2\chi_{O2\_dl}\theta_* - k_{-2}\theta_{O2*}$$

$$r_3 = k_3\theta_{O2*} - k_{-3}\theta_{OOH*}$$

$$r_4 = k_4\theta_{OOH*} - k_{-4}\theta_{O*}\chi_{H2O}$$

$$r_5 = k_5\theta_{O*} - k_{-5}\theta_{OH*}$$

$$r_6 = k_6\theta_{OH*} - k_{-6}\theta_*\chi_{H2O}$$

where χ is mole fraction, θ is coverage of reaction species, and t is time. χ_{O2_aq} and χ_{H2O} are taken as 2.34×10^{-5} and 1, respectively.[22] According to the steady-state approximation, we have:

$$\frac{\partial\chi_{O2\_dl}}{\partial t} = r_1 - r_2 = 0 \tag{10}$$

$$\frac{\partial\theta_{O2*}}{\partial t} = r_2 - r_3 = 0 \tag{11}$$

$$\frac{\partial\theta_{OOH*}}{\partial t} = r_3 - r_4 = 0 \tag{12}$$

$$\frac{\partial\theta_{O*}}{\partial t} = r_4 - r_5 = 0 \tag{13}$$

$$\frac{\partial\theta_{OH*}}{\partial t} = r_5 - r_6 = 0 \tag{14}$$

$$\frac{\partial\theta_*}{\partial t} = r_6 - r_2 = 0 \tag{15}$$

$$\theta_{O2*} + \theta_{OOH*} + \theta_{O*} + \theta_{OH*} + \theta_* = 1 \tag{16}$$

Solve these equations to obtain the potential-dependent coverage and reaction rate. The potential-dependent current density (j), *i.e.* polarization curve, could then be calculated as follows:

$$j = e\rho(r_1 + r_2 + r_3 + r_4) \tag{17}$$

where the ρ is the surface density of active sites. Here, the $e\rho$ is adopted as 80.3 $\mu C/cm^2$.[24]

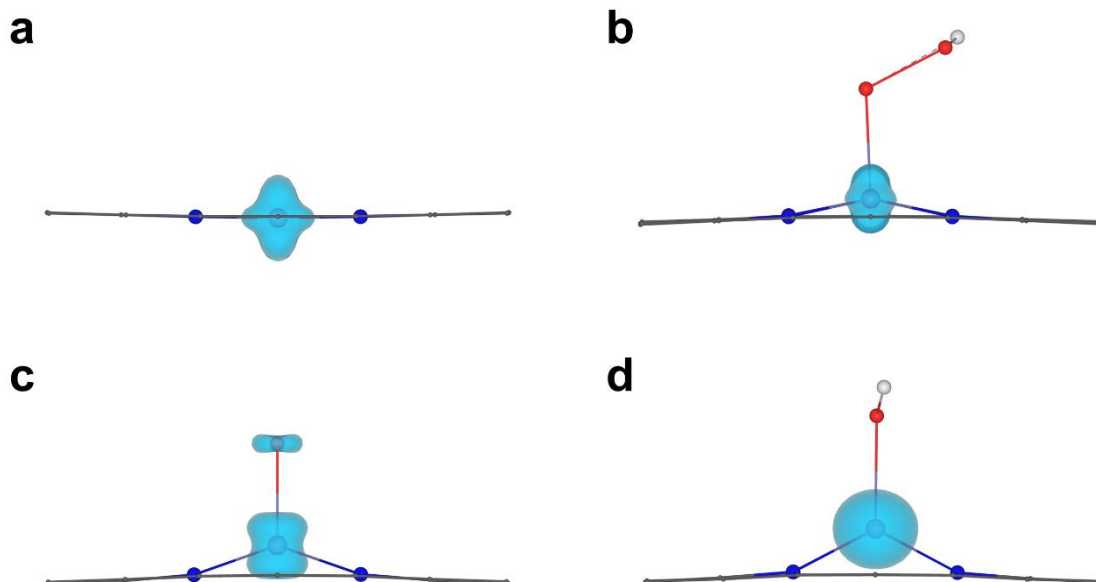**Figure S1.** The spin-charge density of the ground-state **(a)** *, **(b)** OOH*, **(c)** O*, and **(d)** OH* for Fe–N_4–C. The iso-surface is 0.1 e/Bohr^3.

As shown in **Figure S1**, the Fe cations play a major role in the total magnetic moment. The local magnetic moments in the Fe cation were estimated to be 1.88, 1.09, 1.60, and 3.88 μ_B for Fe–N_4–C(*), OOH*, O*, and OH*, respectively, which is close to the number of unpaired d-electrons in medium-spin Fe(II), low-spin Fe(III), medium-spin Fe(IV), and high-spin Fe(III) cations, respectively. Valence orbitals with occupation numbers not close to 1 have different occupation numbers in the two spin channels, and therefore these orbitals will have a small contribution to the local magnetic moment in Fe cations. The local orbital magnetic moment contains the magnetic moments of all valence orbitals, so the value of the local magnetic moment will have a small deviation from the number of unpaired d-electrons.
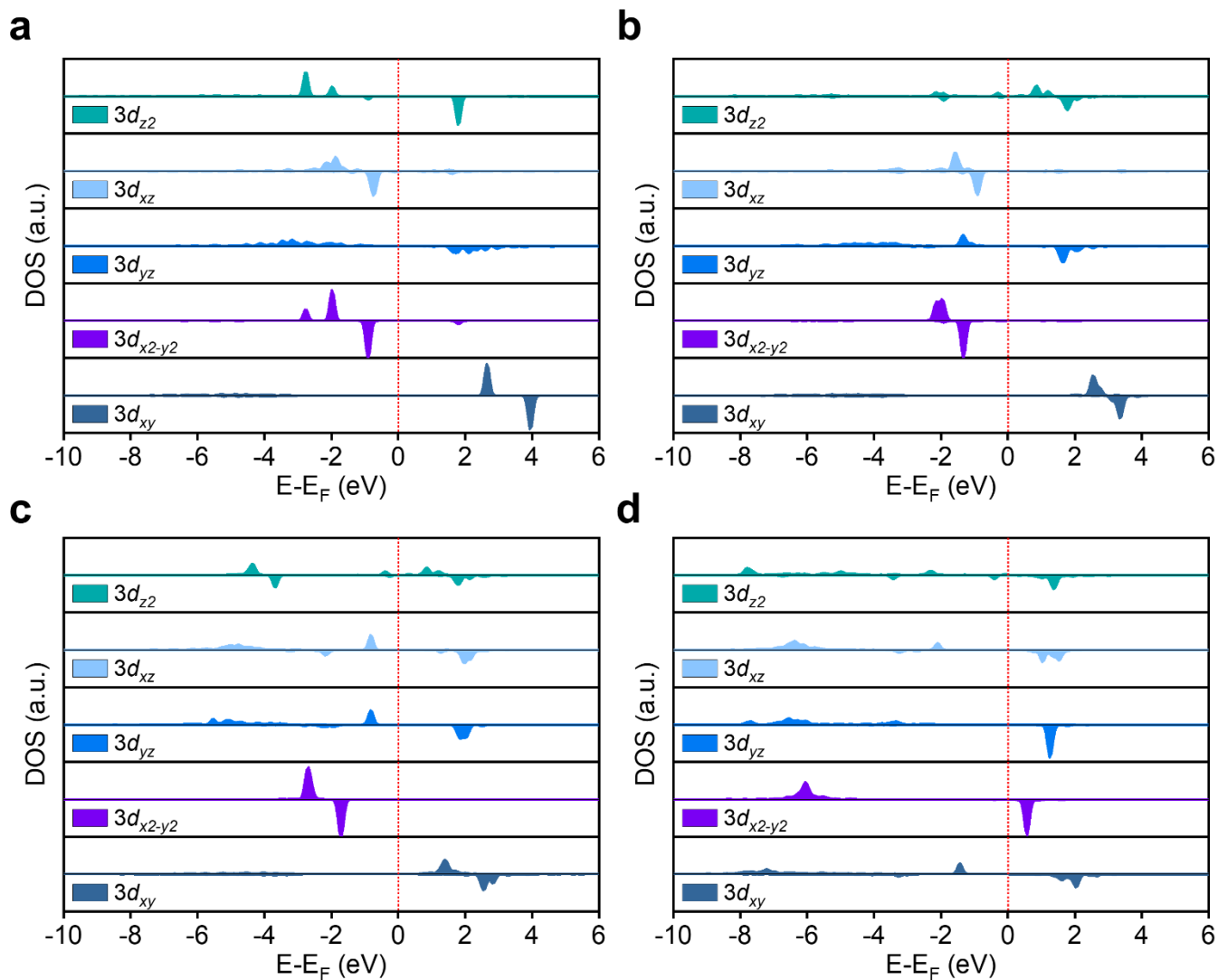
Figure S2. Projected density of states of **(a)** *, **(b)** OOH*, **(c)** O*, and **(d)** OH* for Fe–N$_4$–C. The Fermi level is set to 0 eV.

Considering * as an example, most of the PDOS of spin-up $3d_{z2}$, $3d_{xz}$, $3d_{yz}$, and $3d_{x2-y2}$ orbitals and the spin-down $3d_{xz}$ and $3d_{x2-y2}$ orbitals are below the Fermi level, indicating that these six orbitals are almost fully occupied. This is in good agreement with the results of the SSAdNDP analysis.
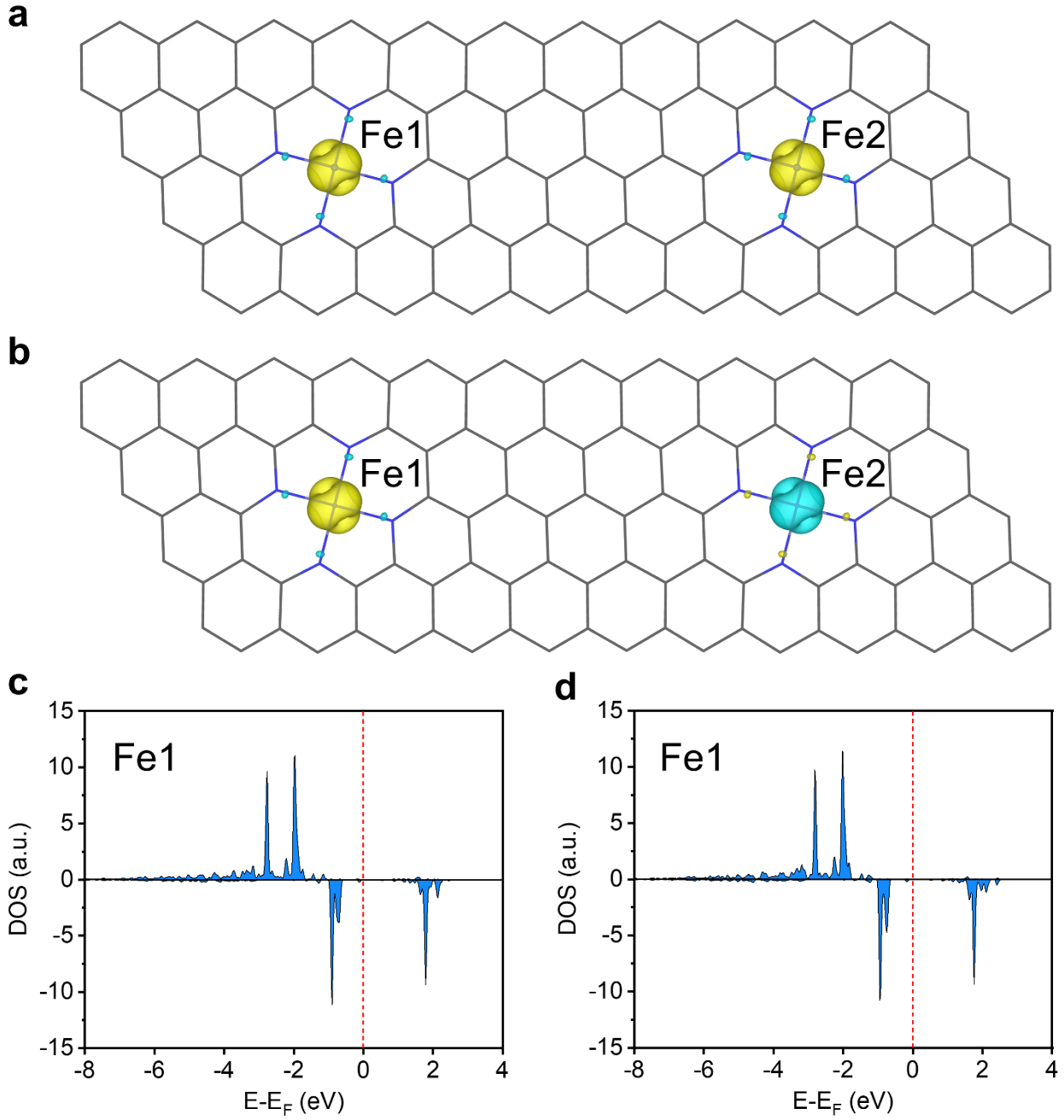
Figure S3. The spin-charge density of $1\times2\times1$ super cell of Fe–N_4–C under (a) ferromagnetic (FM) and (b) antiferromagnetic (AFM) states. The iso-surface is 0.01 e/Bohr^3. The projected density of state of Fe1 cations in Fe–N_4–C under (c) ferromagnetic and (d) antiferromagnetic states.

The effective spin Hamiltonian can be expressed as:

$$H = E_0 + J_1 \sum_{<i,j>} S_i S_j$$

where E_0 is the energy without magnetic coupling, J_1 are the nearest-neighbor exchange parameters, and S is

the unit spin vector. The effective spin Hamiltonian for 1×2×1 super cell of Fe–N_4–C under FM and AFM states are:

$$H_{FM} = E_0 + 6J_1$$

$$H_{AFM} = E_0 - 2J_1$$

, respectively. The calculated H_{FM} and H_{AFM} are -1306.8849 and -1306.8854 eV, respectively. Hence, J_1 is estimated to be -0.06 meV. The J_1 is so small that the DOS of Fe1 atom under FM and AFM state are almost identical.
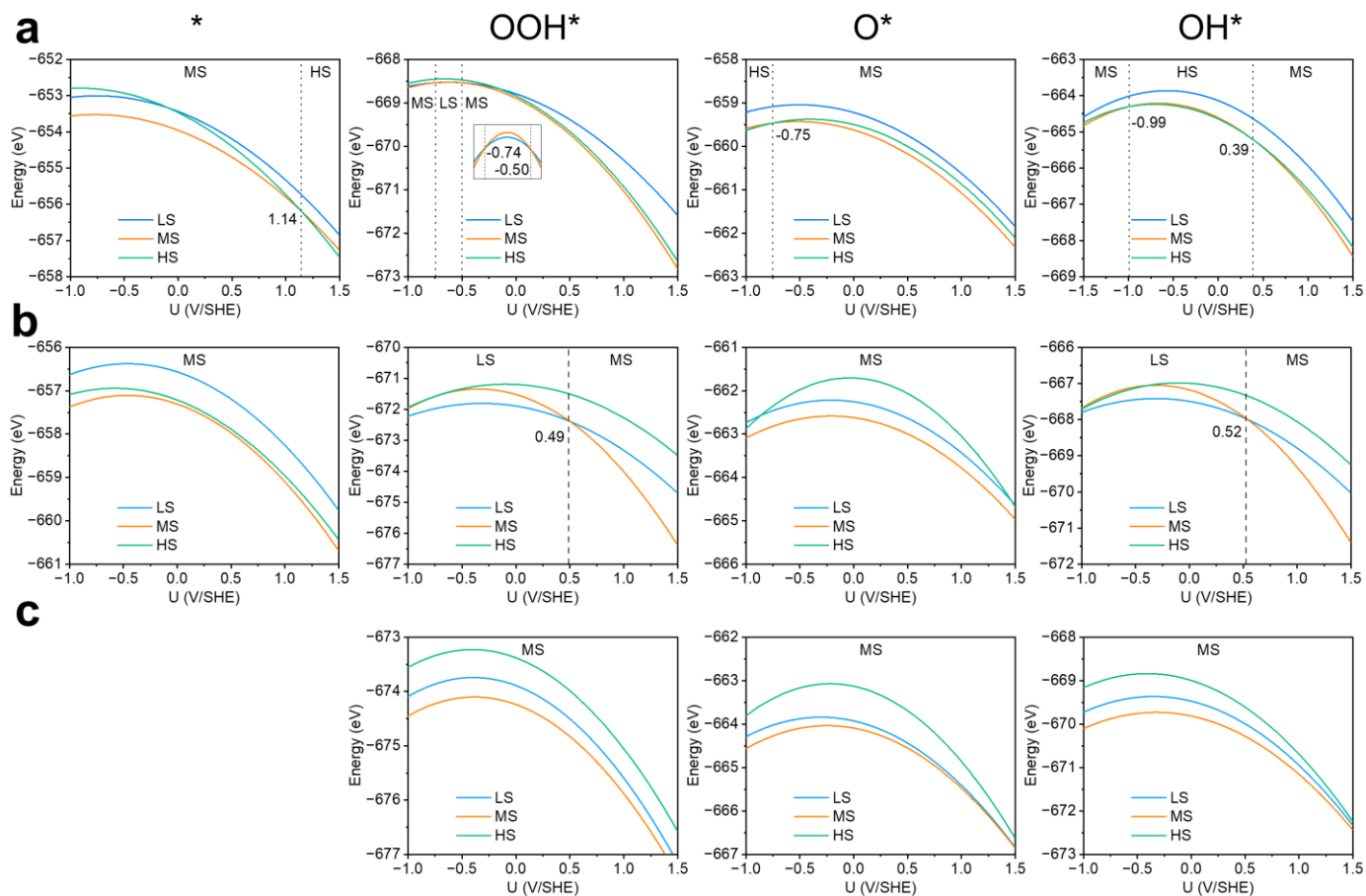
Figure S4. The $E_{free}(U_{SHE})$ of *, OOH*, O*, and OH* systems for (a) Fe–N$_4$–C, (b) Fe–N$_4$Cl–C, and (c) Fe–N$_4$O–C. Note that the * model for Fe–N$_4$O–C is the O* model for Fe–N$_4$–C.
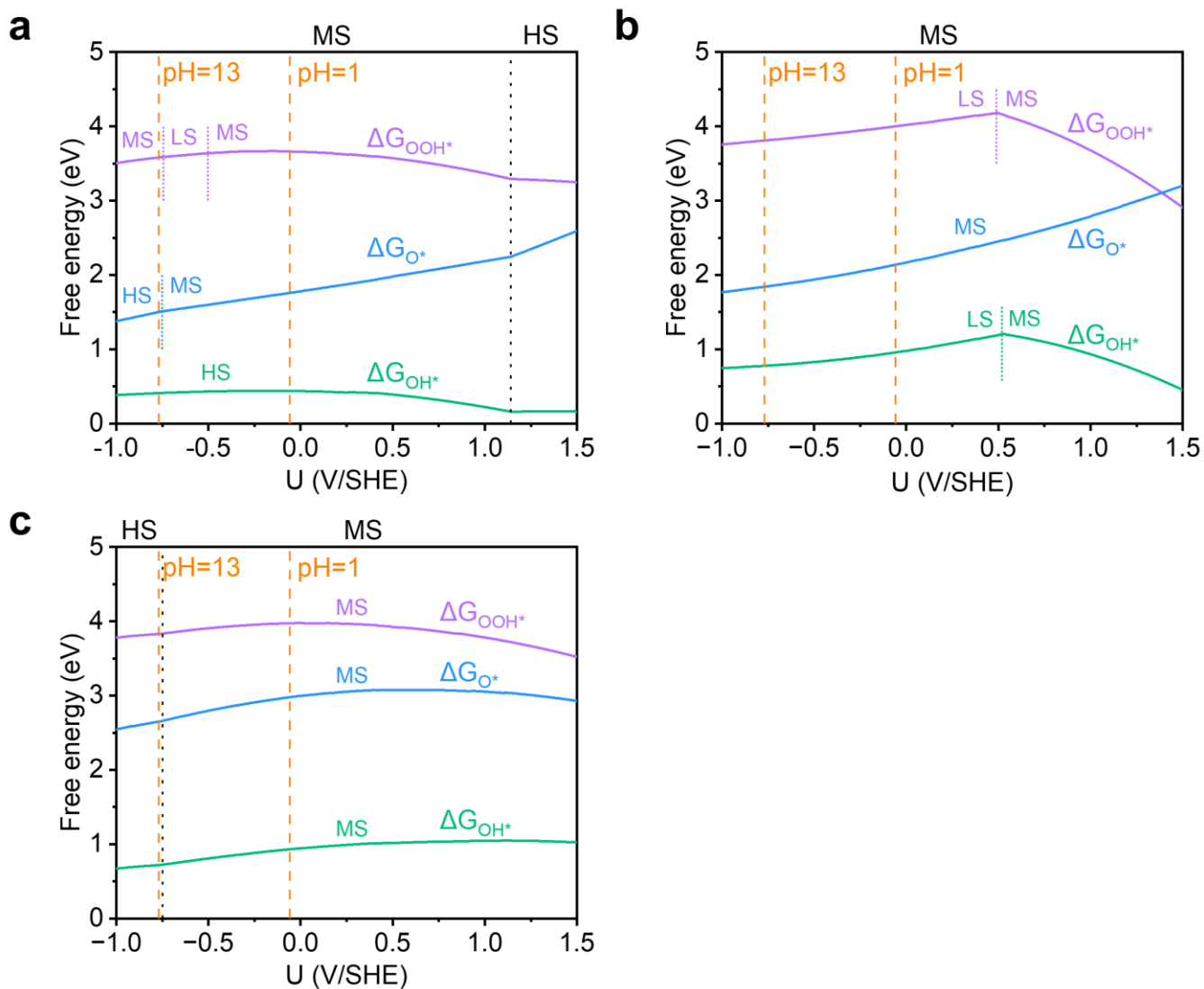
Figure S5. The ΔG_{OOH^*}, ΔG_{O^*}, and ΔG_{OH^*} as a function of electrode potential for (a) Fe–N$_4$–C, (b) Fe–N$_4$Cl–C, and (c) Fe–N$_4$O–C.
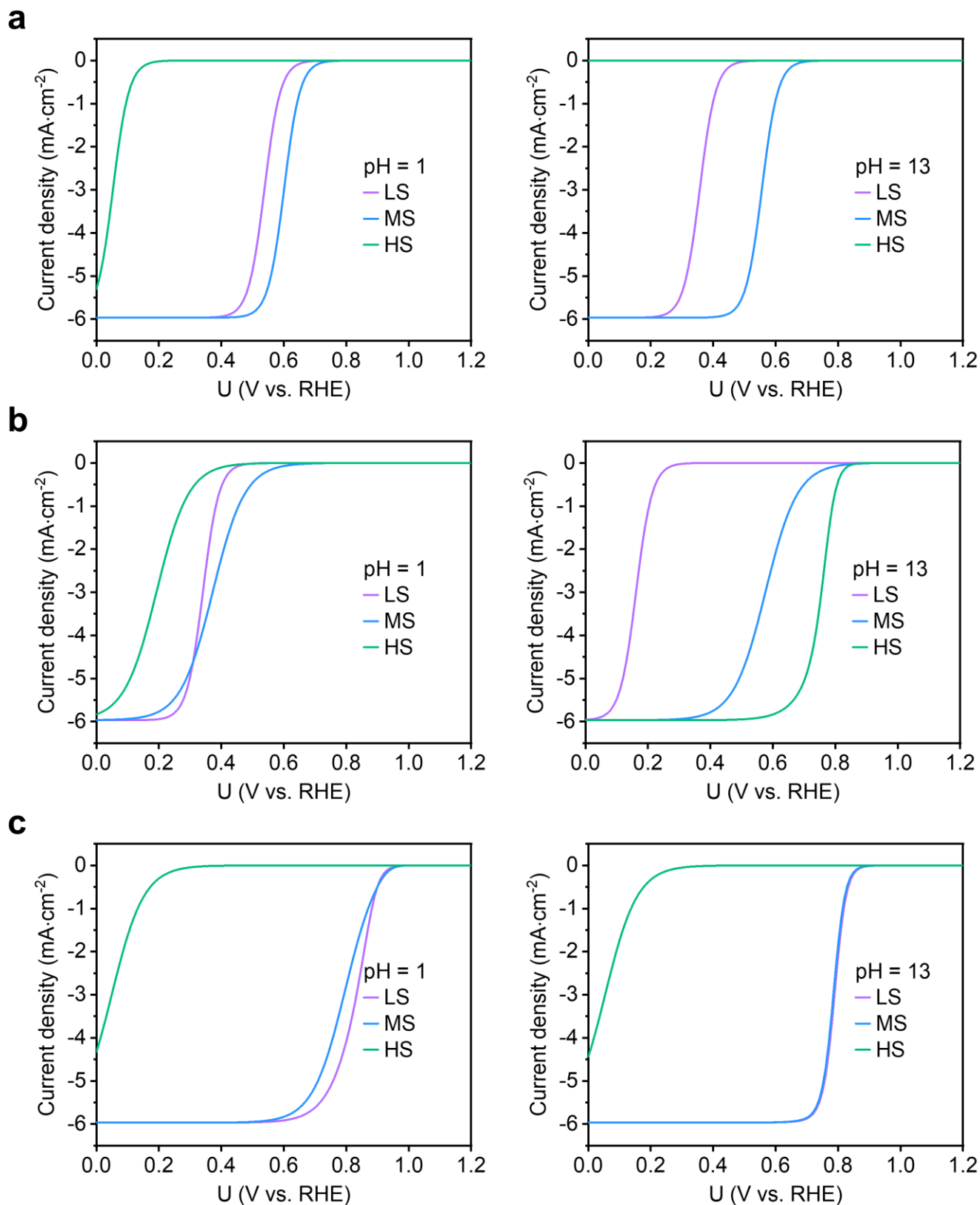
Figure S6. The theoretical polarization curves of LS, MS, HS pathways for (a) Fe–N$_4$–C, (b) Fe–N$_4$Cl–C, and (c) Fe–N$_4$O–C.
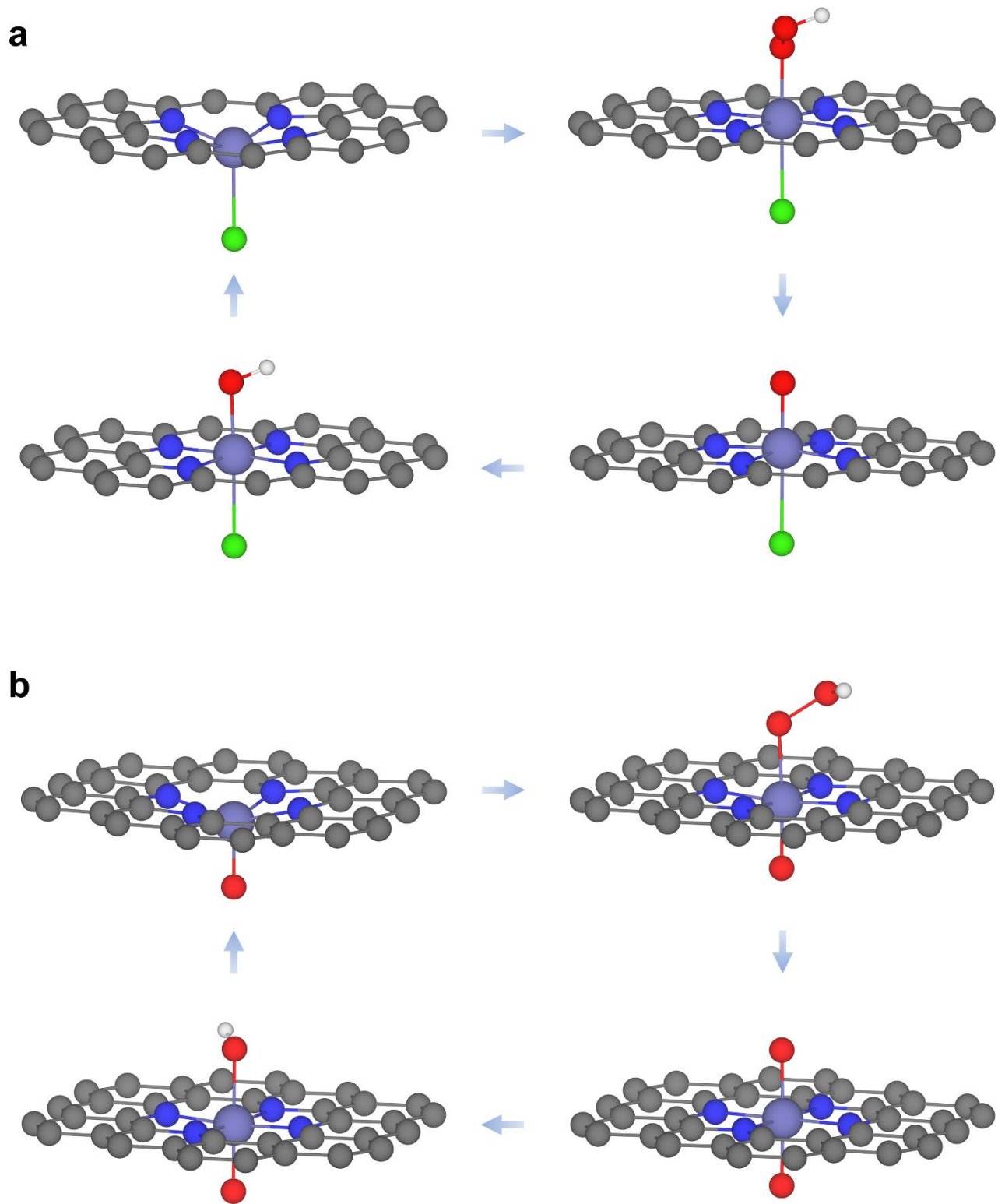
Figure S7. Atomic structures of *, OOH*, O*, and OH* systems for (a) Fe–N₄Cl–C and (b) Fe–N₄O–C. The grey, blue, red, white, purple, and green balls represent C, N, O, H, Fe, and Cl atoms, respectively.
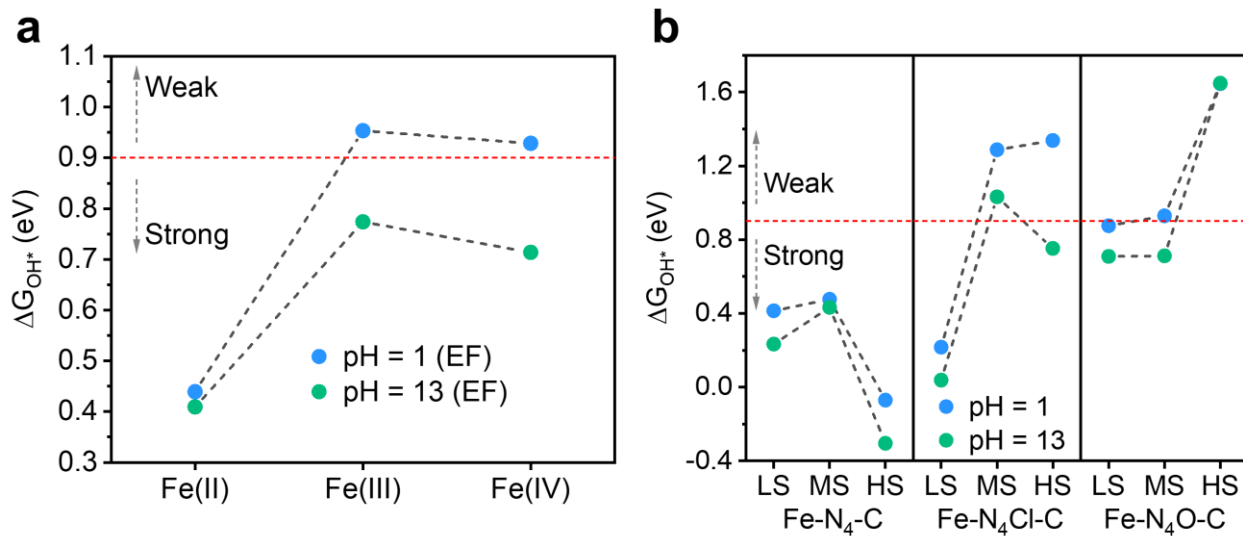
Figure S8. (a) ΔG_{OH*} in EF pathway as a function of valence state of Fe cations in Fe(II)–N$_4$–C, Fe(III)–N$_4$Cl–C, and Fe(IV)–N$_4$O–C. (b) ΔG_{OH*} in LS, MS, and HS pathways as a function of spin state of Fe cations in Fe(II)–N$_4$–C, Fe(III)–N$_4$Cl–C, and Fe(IV)–N$_4$O–C.
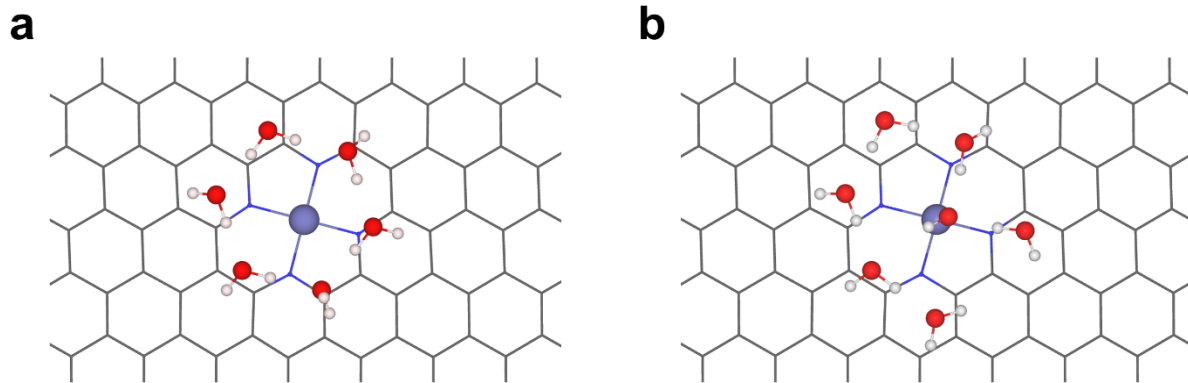
a

b

Figure S9. Explicit solvation model of (a) * and (b) OH* for Fe–N_4–C.

Table S1. Calculated average Fe–N bond length (Å), Fe–O bond length (Å), and N–Fe–O bond angle (°) for Fe–N$_4$–C.

Fe–N$_4$–C	Fe–N bond length	Fe–O bond length	N–Fe–O bond angle
*	1.906	-	-
OOH*	1.919	1.802	98.639
O*	1.978	1.665	103.975
OH*	2.049	1.856	110.286

Fe–N$_4$Cl–C	Fe–N bond length	Fe–O bond length	N–Fe–O bond angle
*	1.967	-	-
OOH*	1.932	1.828	91.027
O*	1.935	1.669	93.617
OH*	1.912	1.859	90.916

Fe–N$_4$O–C	Fe–N bond length	Fe–O bond length	N–Fe–O bond angle
*	1.978	1.665	103.975
OOH*	1.934	1.690	89.999
O*	1.940	1.731	89.991
OH*	1.937	1.687	90.000

Table S2. The energy of various spin states relative to the total energy of the ground state (ΔE_{spin}, meV) for Fe–N$_4$–C.

Fe–N$_4$–C	LS	MS	HS
*	536	0	786
OOH*	0	124	134
O*	396	0	102
OH*	335	5	0

Table S3. The spin up and spin down d-band center (eV) of five d orbitals in *, OOH*, O*, and OH* for Fe–N$_4$–C.

	Spin	$3d_{z2}$	$3d_{xz}$	$3d_{yz}$	$3d_{x2-y2}$	$3d_{xy}$
*	up	-2.38	-1.97	-2.89	-2.18	-0.02
	down	2.13	-0.50	2.33	-0.63	1.71
OOH*	up	-0.81	-1.86	-3.09	-2.03	0.14
	down	0.59	-0.98	1.40	-1.27	1.13
O*	up	-1.84	-3.50	-3.49	-2.64	-0.72
	down	-0.26	0.66	0.78	-1.64	0.85
OH*	up	-5.07	-5.58	-5.55	-5.92	-5.41
	down	0.43	0.56	0.92	0.74	0.52

Table S4. Orbital splitting results (eV) for Fe–N$_4$–C.

	*	OOH*	O*	OH*
Spin-up	2.87	3.23	2.77	0.85
Spin-down	2.96	2.66	2.49	0.49

Table S5. Spin splitting results (eV) for Fe–N$_4$–C.

	$3d_{z2}$	$3d_{xz}$	$3d_{yz}$	$3d_{x2\text{-}y2}$	$3d_{xy}$
*	4.51	1.46	5.23	1.55	1.73
OOH*	1.40	0.88	4.48	0.76	0.99
O*	1.59	4.16	4.27	1.00	1.57
OH*	5.51	6.14	6.48	6.66	5.93

Table S6. The onset potential (E_{onset}, V) and half-wave potential ($E_{1/2}$, V) along various reaction pathways for Fe–N$_4$–C, Fe–N$_4$Cl–C, and Fe–N$_4$O–C.

Fe–N$_4$–C	pH = 1				pH = 13			
	LS	MS	HS	EF	LS	MS	HS	EF
E_{onset}	0.71	0.77	0.22	0.73	0.53	0.73	0.01	0.70
$E_{1/2}$	0.54	0.60	0.06	0.56	0.36	0.56	0.02	0.53

Fe–N$_4$Cl–C	pH = 1				pH = 13			
	LS	MS	HS	EF	LS	MS	HS	EF
E_{onset}	0.51	0.71	0.53	1.01	0.33	0.9	0.88	0.95
$E_{1/2}$	0.34	0.37	0.2	0.77	0.16	0.58	0.76	0.83

Fe–N$_4$O–C	pH = 1				pH = 13			
	LS	MS	HS	EF	LS	MS	HS	EF
E_{onset}	0.98	0.98	0.39	0.98	0.91	0.9	0.39	0.91
$E_{1/2}$	0.83	0.79	0.08	0.79	0.79	0.79	0.08	0.79

Table S7. Occupation number of $4s$ and $3d$ orbitals in Fe cations in Fe–N$_4$Cl–C. The d-electrons assigned to Fe cations are shown in bold.

Spin		Occupation number						State
		$4s$	$3d_{z2}$	$3d_{xz}$	$3d_{yz}$	$3d_{x2-y2}$	$3d_{xy}$	
*	up	0.16	**0.99**	**0.97**	**0.98**	**0.97**	0.51	MS Fe(III)
	down	0.15	0.36	0.17	0.17	**0.97**	0.35	
OOH*	up	0.16	0.48	**0.96**	**0.95**	**0.96**	0.45	LS Fe(III)
	down	0.15	0.41	0.22	**0.94**	**0.97**	0.40	
O*	up	0.16	0.55	**0.97**	**0.97**	**0.96**	0.50	MS Fe(IV)
	down	0.15	0.50	0.44	0.42	**0.97**	0.42	
OH*	up	0.16	0.48	**0.94**	**0.97**	**0.96**	0.45	LS Fe(III)
	down	0.15	0.41	**0.92**	0.21	**0.97**	0.41	

Table S8. Occupation number of $4s$ and $3d$ orbitals in Fe cations in Fe–N_4O–C. The d-electrons assigned to Fe cations are shown in bold.

	Spin	Occupation number						State
		$4s$	$3d_{z2}$	$3d_{xz}$	$3d_{yz}$	$3d_{x2\text{-}y2}$	$3d_{xy}$	
*	up	0.14	0.63	**0.98**	**0.98**	**0.98**	0.46	MS Fe(IV)
	down	0.13	0.46	0.39	0.37	**0.98**	0.36	
OOH*	up	0.15	0.56	**0.97**	**0.97**	**0.97**	0.49	MS Fe(IV)
	down	0.14	0.50	0.41	0.44	**0.97**	0.42	
O*	up	0.15	0.58	**0.85**	**0.97**	**0.97**	0.50	MS Fe(IV)
	down	0.14	0.54	0.47	0.49	**0.97**	0.44	
OH*	up	0.14	0.55	**0.98**	**0.97**	**0.97**	0.50	MS Fe(IV)
	down	0.14	0.50	0.42	0.44	**0.97**	0.42	

References

(1) Perdew, J. P.; Burke, K.; Ernzerhof, M. Generalized Gradient Approximation Made Simple. *Phys. Rev. Lett.* **1996,** *77* (18), 3865–3868.

(2) Kresse, G.; Joubert, D. From ultrasoft pseudopotentials to the projector augmented-wave method. *Phys. Rev. B* **1999,** *59* (3), 1758–1775.

(3) Blöchl, P. E. Projector augmented-wave method. *Phys. Rev. B* **1994,** *50* (24), 17953–17979.

(4) Kresse, G.; Furthmüller, J. Efficient iterative schemes for ab initio total-energy calculations using a plane-wave basis set. *Phys. Rev. B* **1996,** *54* (16), 11169–11186.

(5) Kresse, G.; Furthmüller, J. Efficiency of ab-initio total energy calculations for metals and semiconductors using a plane-wave basis set. *Comput. Mater. Sci.* **1996,** *6* (1), 15–50.

(6) Grimme, S.; Ehrlich, S.; Goerigk, L. Effect of the damping function in dispersion corrected density functional theory. *J. Comput. Chem.* **2011,** *32* (7), 1456–1465.

(7) Mathew, K.; Sundararaman, R.; Letchworth-Weaver, K.; Arias, T. A.; Hennig, R. G. Implicit solvation model for density-functional study of nanocrystal surfaces and reaction pathways. *J. Chem. Phys.* **2014,** *140* (8), 084106.

(8) Mathew, K.; Kolluru, V. S. C.; Mula, S.; Steinmann, S. N.; Hennig, R. G. Implicit self-consistent electrolyte model in plane-wave density-functional theory. *J. Chem. Phys.* **2019,** *151* (23), 234101.

(9) Pritchard, B. P.; Altarawy, D.; Didier, B.; Gibson, T. D.; Windus, T. L. New Basis Set Exchange: An Open, Up-to-Date Resource for the Molecular Sciences Community. *J. Chem. Inf. Model.* **2019,** *59* (11), 4814–4820.

(10) Galeev, T. R.; Dunnington, B. D.; Schmidt, J. R.; Boldyrev, A. I. Solid state adaptive natural density partitioning: a tool for deciphering multi-center bonding in periodic systems. *Phys. Chem. Chem. Phys.* **2013,** *15* (14), 5022–5029.

(11) Wang, V.; Xu, N.; Liu, J.-C.; Tang, G.; Geng, W.-T. VASPKIT: A user-friendly interface facilitating high-throughput computing and analysis using VASP code. *Comput. Phys. Commun* **2021,** *267*, 108033.

(12) Momma, K.; Izumi, F. VESTA3 for three-dimensional visualization of crystal, volumetric and morphology data. *J. Appl. Crystallogr.* **2011,** *44* (6), 1272–1276.

(13) Panchmatia, P. M.; Sanyal, B.; Oppeneer, P. M. GGA+U modeling of structural, electronic, and magnetic properties of iron porphyrin-type molecules. *Chem. Phys.* **2008,** *343* (1), 47–60.

(14) Nørskov, J. K.; Rossmeisl, J.; Logadottir, A.; Lindqvist, L.; Kitchin, J. R.; Bligaard, T.; Jónsson, H. Origin of the Overpotential for Oxygen Reduction at a Fuel-Cell Cathode. *J. Phys. Chem. B* **2004,** *108* (46), 17886–17892.

(15) Duan, Z.; Henkelman, G. Theoretical Resolution of the Exceptional Oxygen Reduction Activity of Au(100) in Alkaline Media. *ACS Catal.* **2019,** *9* (6), 5567-5573.

(16) Allen, J. P.; Watson, G. W. Occupation matrix control of d- and f-electron localisations using DFT + U. *Phys. Chem. Chem. Phys.* **2014,** *16* (39), 21016-21031.

(17) Filhol, J.-S.; Neurock, M. Elucidation of the Electrochemical Activation of Water over Pd by First Principles. *Angew. Chem., Int. Ed.* **2006,** *45* (3), 402-406.

(18) Hansen, H. A.; Viswanathan, V.; Nørskov, J. K. Unifying Kinetic and Thermodynamic Analysis of 2 e– and 4 e– Reduction of Oxygen on Metal Surfaces. *J. Phys. Chem. C* **2014,** *118* (13), 6706-6718.

(19) Huang, X.; Gan, L.-Y.; Wang, J.; Ali, S.; He, C.-C.; Xu, H. Developing Proton-Conductive Metal Coordination Polymer as Highly Efficient Electrocatalyst toward Oxygen Reduction. *J. Phys. Chem. Lett.* **2021,** *12* (38), 9197-9204.

(20) Liu, T.; Jing, Y.; Li, Y. Two-Dimensional Biphenylene: A Graphene Allotrope with Superior Activity toward Electrochemical Oxygen Reduction Reaction. *J. Phys. Chem. Lett.* **2021**, 12230-12234.

(21) Tripković, V.; Skúlason, E.; Siahrostami, S.; Nørskov, J. K.; Rossmeisl, J. The oxygen reduction

reaction mechanism on Pt(111) from density functional theory calculations. *Electrochim. Acta* **2010,** *55* (27), 7975-7981.

(22) Liu, S.; White, M. G.; Liu, P. Mechanism of Oxygen Reduction Reaction on Pt(111) in Alkaline Solution: Importance of Chemisorbed Water on Surface. *J. Phys. Chem. C* **2016,** *120* (28), 15288-15298.

(23) Li, H.; Kelly, S.; Guevarra, D.; Wang, Z.; Wang, Y.; Haber, J. A.; Anand, M.; Gunasooriya, G. T. K. K.; Abraham, C. S.; Vijay, S.; Gregoire, J. M.; Nørskov, J. K. Analysis of the limitations in the oxygen reduction activity of transition metal oxide surfaces. *Nat. Catal.* **2021,** *4* (6), 463–468.

(24) Wang, J. X.; Markovic, N. M.; Adzic, R. R. Kinetic Analysis of Oxygen Reduction on Pt(111) in Acid Solutions: Intrinsic Kinetic Parameters and Anion Adsorption Effects. *J. Phys. Chem. B* **2004,** *108* (13), 4127-4133.